https://doi.org/10.1016/j.cma.2021.114179 **This is the Pre-Published Version.**

A stable node-based smoothed PFEM for solving geotechnical large deformation 2D problems

Yin-Fu JIN[1], Zhen-Yu YIN[1*], Xi-Wen ZHOU[2] and Feng-Tao LIU[2*]

Affiliation:

1 Department of Civil and Environmental Engineering, The Hong Kong Polytechnic University, Hung Hom, Kowloon, Hong Kong

2 School of Earth Science and Engineering, Sun Yat-Sen University, Guangzhou 510275, China.

* Corresponding author: Dr Zhen-Yu Yin, Tel. +852 34008470, Fax +852 23346389, E-mail: zhenyu.yin@polyu.edu.hk; Dr. Feng-Tao Liu, +86 755 3668226, Email: liuft@mail.sysu.edu.cn

Abstract: The strain smoothed nodal integration particle finite element method (NS-PFEM) has a high level of computational efficiency. However, it suffers from the 'overly soft' problem ~~and has not yet been extended to hydromechanical coupling~~. This study presents the development of a stable nodal integration PFEM for solving ~~hydromechanical coupled~~ geotechnical large deformation problems. ~~First, a~~ A node-based strain smoothing (SNS) PFEM is developed by combining a 3-node triangular element–based PFEM and a stable nodal integration method with strain gradient in the smooth domain for single solid phase. Its performance is examined by simulating two benchmark tests on elastic material (i.e., cantilever beam and infinite plate with a circular hole) and three cases on elastoplastic material (i.e., cavity expansion, penetration of a rigid footing in soft soil and progressive failure of slope). Results show that the integration of stabilisation term gives the SNS-PFEM 'close to exact' stiffness, thereby resolving the 'overly soft' and temporal instability issues seen with the NS-PFEM. ~~Secondly, a novel efficient water pressure stabilisation scheme based on an inverse distance interpolation algorithm (IDA) is proposed to cure spurious spatial water pressure oscillations, allowing the development of a hydromechanical coupling method. The performance of the hydromechanical SNS-PFEM is primarily validated by both static and dynamic consolidation cases, and then applied to simulate the Selborne cutting slope experiment. All results demonstrate that~~ The proposed method is powerful and easily extensible for analysing large deformation problems in geotechnical engineering.

Key words: stabilization; PFEM; strain smoothing; large deformation; slope failure; footing

1 Introduction

The particle finite element method (PFEM), first developed to solve fluid–structure interaction problems [1, 2], has recently been used to solve problems in geomechanics [3-9]. The PFEM is actually an updated Lagrangian approach that uses frequent remeshing based on the Delaunay triangulation technique to overcome mesh distortion problems. This approach inherits both the flexibility of mesh-free particle methods for arbitrary changes in geometry and the solid mathematical foundation of the traditional FEM. For the original PFEM, the 6-node (quadratic) triangular element is adopted that is traditionally used in geotechnical applications [3, 5, 10, 11], producing more degrees of freedom than lower-order triangular elements. Furthermore, frequent variable mapping (e.g., stress, strain and state variables) between the old mesh and the newly generated mesh is problematic, greatly increasing computational cost and reducing calculation accuracy.

To overcome the aforementioned problems, combinations of various strain smoothing techniques with lower-order elements have been proposed, such as the node-based smoothed PFEM (NS-PFEM) [12-16] and edge-based smoothed PFEM (ES-PFEM) [17, 18]. The NS-PFEM has its advantages – no need for variable mapping and no volumetric locking – but its 'overly soft' property, which leads to temporal instability that can seriously degrade the accuracy of the simulation's results, is a serious obstacle to its further application in large deformation problems [13-16, 19, 20]. Although the ES-PFEM offers remarkable and indeed superior convergence properties, computational accuracy and efficiency, spatial and temporal stability, it is associated with frequent variable mapping. Overall, the NS-PFEM's high level of computational efficiency would make it more advantageous than the ES-PFEM if its 'overly soft' property could be addressed.

To eliminate the NS-FEM's temporal instability, various stabilisation techniques have been developed: (1) a hybrid of the FEM and the NS-FEM with an adjustable stabilisation parameter (αFEM [21]); (2) application of a gradient smoothing operation to second-order derivatives, to relax the shape function requirement using an adjustable stabilisation parameter [22]; (3) a stabilisation formulation with multiple nodal stress points [23, 24]; and (4) a stable node-based smoothed finite

element method (SNS-FEM) with strain gradient [19, 20, 25-27]. Among these, the SNS-FEM with strain gradient achieves appropriate system stiffness in strain energy between the FEM and NS-FEM solutions, providing temporally stable results [28]. However, this stabilisation method has not been used to enhance the performance of the NS-PFEM, nor has it been applied to geotechnical large deformation problems.

~~Besides, geotechnical failures or hazards are always associated with the change of pore water pressure, such as landslides due to rainfall [29-31] and excavation/tunnel collapse [32-34]. Similarly, failures of earthworks (e.g. levees, dikes, and embankments) occur mainly due to seepage flows induced by intense rainfall or flooding [35-38]. In these cases, accurately simulating such hydromechanical problems is crucial to reduce the risk of disaster, and thus reduce the loss of life and property. To solve such coupled problem involving large deformation, some typical methods have been developed and widely used, such as the coupled material point method (MPM) [39-43], the coupled smoothed particle hydrodynamics (SPH) [44], the coupled PFEM [6, 7, 45] and other coupled meshfree methods [46-51]. In comparison to other approaches, if the NS-PFEM is successfully stabilized, it will have more advantages because of adopting the lower-order triangular element without suffering volumetric locking and nodal integration. Thus, it is worth being extended to hydromechanical coupling analysis.~~

This study ~~first~~ proposes a stable NS-PFEM (SNS-PFEM) that incorporates a stable nodal integration method with strain gradient into the NS-PFEM. In each smoothing domain, an additional term related to strain gradient is incorporated as a stabilisation term. The proposed SNS-PFEM still adopts the 3-node triangle elements with an explicit time integration scheme. Two classical geotechnical large deformation problems are analysed to verify the correctness of the program's implementation and the effectiveness of the stabilisation term's introduction: two benchmark tests on elastic material and three cases on elastoplastic material. ~~Secondly, a coupled hydromechanical SNS-PFEM with v-w formulation is developed. The performance of the proposed coupled SNS-PFEM is then validated by three cases: (1) a 1D consolidation test, (2) a 1D dynamic consolidation test and (3) 2D wave propagation. Finally, the proposed coupled SNS-PFEM is applied to simulate the Selborne cutting slope experiment.~~

2 Stable node-based strain smoothed PFEM

2.1 Governing equations

2.1.1 *Strong form*

The strong form of the equilibrium equation can be expressed as

$$\operatorname{div}\boldsymbol{\sigma}+\rho\mathbf{g}-\rho\mathbf{a}=\mathbf{0} \tag{1}$$

with the boundary conditions

$$\begin{cases}\mathbf{u}=\bar{\mathbf{u}} & \text{in } \boldsymbol{\Gamma}_{\mathbf{u}}\\ \boldsymbol{\sigma}\cdot\mathbf{n}=\bar{\mathbf{t}} & \text{in } \boldsymbol{\Gamma}_{\mathbf{t}}\end{cases} \tag{2}$$

where ρ is the material density, $\mathbf{a}=\ddot{\mathbf{u}}$ the acceleration, $\mathbf{g}$ the acceleration due to gravity, $\mathbf{n}$ the outward unit vector at the boundary of the body, and $\boldsymbol{\Gamma}_{\mathbf{u}}$ and $\boldsymbol{\Gamma}_{\mathbf{t}}$ the boundaries of the domain where displacements $\mathbf{u}$ and tractions $\bar{\mathbf{t}}$ are prescribed.

The stress can be updated to

$$\boldsymbol{\sigma}^{k+1}=\boldsymbol{\sigma}^{k}+\Delta\boldsymbol{\sigma}^{k} \tag{3}$$

Via the constitutive relation, the increment of stress $\Delta\boldsymbol{\sigma}^{k}$ can be calculated as

$$\Delta\boldsymbol{\sigma}^{k}=\mathbf{D}_{ep}:\Delta\boldsymbol{\varepsilon}^{k} \tag{4}$$

where $\mathbf{D}_{ep}$ is the material elasto-plastic tangent stiffness tensor and $\Delta\boldsymbol{\varepsilon}^{k}$ the increment of strain tensor at k time step.

When simulating large deformation, the Jaumann stress rate should be considered [29]. Thus the stress tensor is updated to

$$\boldsymbol{\sigma}^{k+1}=\boldsymbol{\sigma}^{k}+\Delta t\left(\dot{\mathbf{w}}\cdot\boldsymbol{\sigma}^{k}-\boldsymbol{\sigma}^{k}\cdot\dot{\mathbf{w}}\right)+\mathbf{D}_{ep}:\Delta\boldsymbol{\varepsilon}^{k} \tag{5}$$

where $\mathbf{w}$ is the spin tensor, defined with velocity $\mathbf{v}$ as

$$\mathbf{w}=\frac{1}{2}\left(\nabla\mathbf{v}-\left(\nabla\mathbf{v}\right)^{T}\right) \tag{6}$$

2.1.2 *Weak form and discretisation*

According to the principle of minimum potential energy, the equilibrium conditions are equivalent to the extreme condition of total potential energy functional, i.e.,

$$\delta\Pi_{P}=\int_{\Omega}\left[\frac{\partial A}{\partial\boldsymbol{\varepsilon}}\delta\nabla\mathbf{u}-\left(\rho\mathbf{g}-\rho\mathbf{a}\right)^{T}\delta\mathbf{u}\right]d\Omega-\int_{\Gamma_{t}}\bar{\mathbf{t}}^{T}\delta\mathbf{u}dS=0 \tag{7}$$

where $A(\boldsymbol{\varepsilon})$ is strain energy, $\bar{\mathbf{t}}$ is the prescribed traction, $\mathbf{u}$ denotes the displacement field, assumed to satisfy where the displacement boundary conditions are prescribed. Furthermore, substituting the discretized displacement and strain field $\mathbf{u}=\mathbf{N}\mathbf{u}_{I}$, $\boldsymbol{\varepsilon}=\mathbf{B}\mathbf{u}_{I}$ into Eq.(7), and applying the divergence theorem and considering the arbitrariness of the variation of nodal displacement $\delta\mathbf{u}_{I}$, the final semi-discrete form is formulated as follows

$$\sum_{e=1}^{N_e}\int_{\Omega_e}\rho\mathbf{g}^{T}\mathbf{N}d\Omega+\sum_{e=1}^{N_{\Gamma_t}}\int_{\Gamma_t^e}\bar{\mathbf{t}}^{T}\mathbf{N}dS=\sum_{e=1}^{N_e}\int_{\Omega_e}\mathbf{B}^{T}\boldsymbol{\sigma}d\Omega+\mathbf{a}\sum_{e=1}^{N_e}\int_{\Omega_e}\mathbf{N}^{T}\rho\mathbf{N}d\Omega \tag{8}$$

where N_e is the number of elements, $\mathbf{B}$ the strain–displacement matrix, $\mathbf{N}$ the shape function and $\mathbf{u}_{I}$ the nodal displacement vector. The foregoing equation can also be written in matrix form as

$$\mathbf{M}\mathbf{a}=\mathbf{F}^{\text{ext}}-\mathbf{F}^{\text{int}} \tag{9}$$

where $\mathbf{M}=\rho\int_{\Omega}\mathbf{N}^{T}\mathbf{N}d\Omega$ is the mass matrix, $\mathbf{F}^{\text{ext}}$ the external force and $\mathbf{F}^{\text{int}}=\int_{\Omega}\mathbf{B}^{\mathrm{T}}\boldsymbol{\sigma}d\Omega$ the internal force. The central differential time integration and adaptive time step are used to solve this dynamic system [17, 18, 30]. When the implicit scheme (e.g., Newton-Raphson) is used for static problem, the global stiffness matrix is a key variable and can be expressed as

$$\mathbf{K}=\int_{\Omega}\mathbf{B}\mathbf{D}\mathbf{B}d\Omega \tag{10}$$

2.2 Stable nodal integration scheme with strain gradient

2.2.1 *Node-based strain smoothing method*

Strain smoothing is first proposed to stabilise nodal integration [31, 32]. As Fig. 1 illustrates, the problem domain Ω is divided into a set of N_n non-overlapping smoothing domains with no gap between. The smoothing cell for particle k is created by sequentially connecting the midpoint of each edge to the centre of the surrounding triangular elements associated with particle k. Thus the strain tensor $\tilde{\boldsymbol{\varepsilon}}_k$ for particle k (i.e., the smoothed strain on cell Ω^k) can be obtained as

$$\tilde{\boldsymbol{\varepsilon}}_k = \frac{1}{A_k^s}\sum_{I=1}^{N^k}\int_{\Omega_k^s}\mathbf{B}_I\mathbf{u}_I d\Omega_k^s = \frac{1}{A_k^s}\sum_{I=1}^{N^k}\int_{\Omega_k^s}\mathbf{B}_I d\Omega_k^s\mathbf{u}_I = \sum_{I\notin N^k}\tilde{\mathbf{B}}_I(x^k)\mathbf{u}_I \tag{11}$$

where I is the node number, A_k^s the area of the smooth domain, x the coordinate, N^k the number of nodes directly connected to particle k, and $\tilde{\mathbf{B}}_I$ the smoothed strain–displacement matrix of node *I*, which can be calculated as

$$\begin{aligned}\tilde{\mathbf{B}}_I &= \frac{1}{A_k^s}\int_{\Omega_k^s}\begin{bmatrix}\frac{\partial N_I}{\partial x} & 0\\ 0 & \frac{\partial N_I}{\partial y}\\ \frac{\partial N_I}{\partial y} & \frac{\partial N_I}{\partial x}\end{bmatrix}d\Omega_k^s = \frac{1}{A_k^s}\int_{\Gamma_k^s}\begin{bmatrix}N_I n_x & 0\\ 0 & N_I n_y\\ N_I n_y & N_I n_x\end{bmatrix}d\Gamma_k^s\\ &= \frac{1}{A_k^s}\begin{cases}\int_{\Gamma_k^s}N_I n_x d\Gamma_k^s = \frac{1}{A_k^s}\sum_{seg=1}^{M}N_I(x_{seg}^{GP})n_x l_{seg}\\ \int_{\Gamma_k^s}N_I n_y d\Gamma_k^s = \frac{1}{A_k^s}\sum_{seg=1}^{M}N_I(x_{seg}^{GP})n_y l_{seg}\end{cases}\end{aligned} \tag{12}$$

where N_{I} is the shape function related to particle *I*; *M* the total number of the boundary segment of Γ_k^s; and x_{seg}^{GP} the Gauss point of the boundary segment of $\left(\Gamma_k^s\right)_{seg}$, which has length l_{seg} and outward unit normal n_{x} and n_{y}.

Adopting the node-based strain smoothing in the FEM, the internal force vectors can be expressed as

$$\mathbf{F}^{\text{int}}=\int_{\Omega}\tilde{\mathbf{B}}^{\mathrm{T}}\cdot\bar{\boldsymbol{\sigma}}\,d\Omega=\sum_{k=1}^{N_n}\tilde{\mathbf{B}}_{\mathrm{k}}{}^{\mathrm{T}}\cdot\bar{\boldsymbol{\sigma}}\,A_k^s \tag{13}$$

where $\bar{\boldsymbol{\sigma}}=\mathbf{D}^{ep}\tilde{\boldsymbol{\varepsilon}}$ is the stress tensor at the node. For a smoothing domain, the nodal integration of internal force is conducted at the node. The material parameters of constitutive model are assigned to node instead of the Gauss point of elemental integration. When the elements in smoothing patch have different material properties, only the information at the node (e.g., node k in Fig. 1) is used for integration. $\tilde{\mathbf{B}}_{\mathrm{k}}=\left[\tilde{\mathbf{B}}_1 \quad \tilde{\mathbf{B}}_2 \quad \ldots \quad \tilde{\mathbf{B}}_I\right]$ is the smoothed strain–displacement matrix of smooth cell of k. The global stiffness matrix is expressed as:

$$\mathbf{K}=\int_{\Omega}\tilde{\mathbf{B}}^{\mathrm{T}}\mathbf{D}\tilde{\mathbf{B}}d\Omega=\sum_{k=1}^{N_n}\mathbf{K}_k=\sum_{k=1}^{N_n}\tilde{\mathbf{B}}_{\mathrm{k}}{}^{\mathrm{T}}\mathbf{D}\tilde{\mathbf{B}}_{\mathrm{k}}A_k^s \tag{14}$$

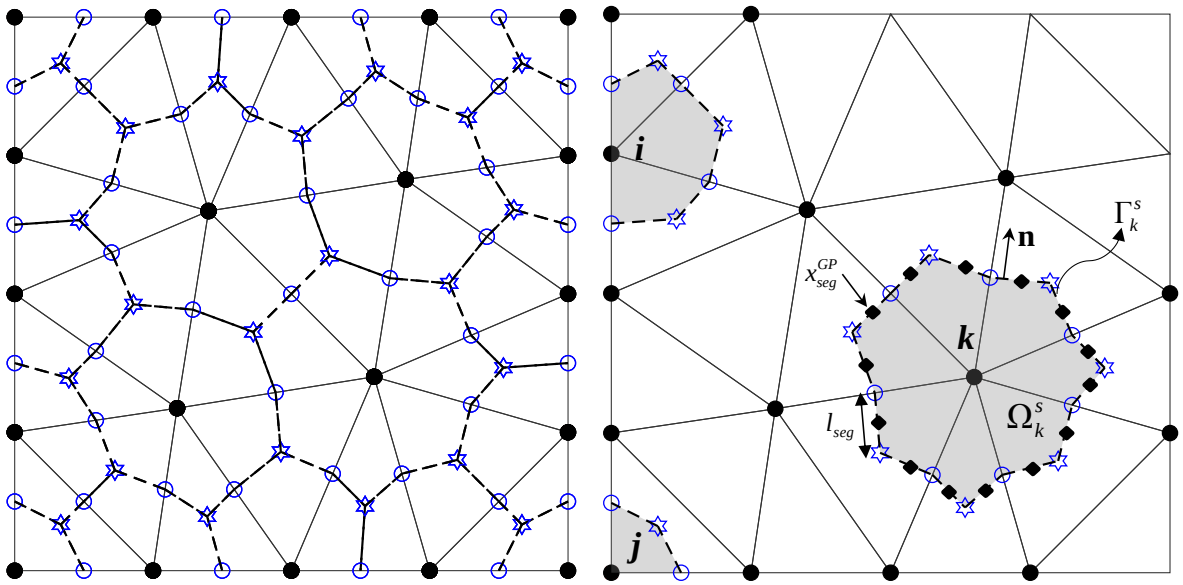

Fig. 1 Schematic of a 2D smoothing domain for NS-PFEM

Numerical applications [12, 14, 15] have shown that the NS-PFEM has two drawbacks: (1) "overly soft" or underestimation property, which gives upper-bound solutions in strain energy (for force-driven problems). Since the number of smoothing domains relating to node number for NS-PFEM is less than the number associated with element number (T3-PFEM), the NS-PFEM

solution is softer than exact one according to the weakened weak (W^2) formulation theory [33]. The detailed proof procedure can be found in [33, 34]; (2) temporal instability, which is defined as models that have spurious non-zero eigen modes for free vibrations [22]. According to Zeng and Liu [35], for dynamic problems, the mass matrix in addition to the stiffness matrix is additionally added in the governing equations. Therefore, there is a competition between the eigenvalues of the stiffness matrix and the mass matrix. In NS-PFEM, the stiffness is reduced quite significantly due to the overly-soft behaviour, and hence the eigenvalues for some modes could be (relatively) lower than that of the mass matrix. Such modes are observed as the non-zero-energy spurious modes. The instability does not influence the calculation of the statics problem, but, it will affect the time-dependent analysis (e.g., dynamics problems [25], large deformation problems [12, 13, 17, 36]). The temporal instability can lead to the discontinuous and point shape distribution of stress [36]. In the following sections, the aforementioned phenomena of NS-PFEM on various problems with elastic and elastoplastic materials will be presented.

2.2.2 *Stable node-based strain smoothing approach*

To further stabilise nodal integration, various stable techniques have been proposed [37] that have been applied to various problems [25, 27, 38, 39]. According to [25, 37], assuming that smooth domain Ω_k^{sc} can be approximated as a circle for 2D problems (or a sphere for 3D problems). In this study, the 2D problem is given more attention. It is subdivided into four sub-domains, with the selected integration points g_i^n (i=1, 2, 3 and 4) lying on the x-axis and y-axis and maintaining the same distance l_c to node k, as Fig. 2 shows. l_c is the radius of domain Ω_k^{sc} with the area A_k^s, which can be calculated as

$$l_c = \sqrt{A_k^s / \pi} \tag{15}$$

Note that when the node at boundary, the radius of the circle is also calculated by the area of smoothing domain using Eq.(15). No additional treatment is needed.

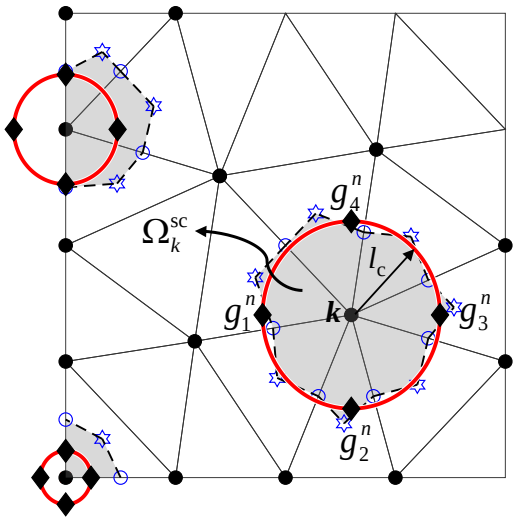

Fig. 2 Schematic of a 2D integration domain for the SNS-PFEM

Assuming that strain in Ω_k^{sc} is continuous and derivable at the first order, its Taylor expansion is

$$\boldsymbol{\varepsilon} = \boldsymbol{\varepsilon}_k + \frac{\partial \boldsymbol{\varepsilon}}{\partial x}\left(x - x_k\right) + \frac{\partial \boldsymbol{\varepsilon}}{\partial y}\left(y - y_k\right) \tag{16}$$

where $\boldsymbol{\varepsilon}_k$ is the smoothed strain of node *k*; $\frac{\partial \boldsymbol{\varepsilon}}{\partial x}$ and $\frac{\partial \boldsymbol{\varepsilon}}{\partial y}$ the strain gradient along the *x*-axis and *y*-axis, respectively; and (x_k, y_k) the coordinate of node *k*. Here we replace Eq. (16) with the gradient smoothing technique, to obtain

$$\tilde{\boldsymbol{\varepsilon}} = \tilde{\boldsymbol{\varepsilon}}_k + \boldsymbol{\varepsilon}_{kx}^{'}\left(x - x_k\right) + \boldsymbol{\varepsilon}_{ky}^{'}\left(y - y_k\right) \tag{17}$$

For this stabilised technique, the key point is to calculate the smoothed strain gradient $\boldsymbol{\varepsilon}_{kx}^{'}$ and $\boldsymbol{\varepsilon}_{ky}^{'}$. Much as in Eq. (12), the smoothed strain gradient is calculated by integrating the first derivatives of the shape function on the boundary of smooth domain as follows:

$$\begin{aligned} \boldsymbol{\varepsilon}_{kx}^{'} &= \frac{1}{A_k^s}\int_{\Omega_k^s}\frac{\partial \boldsymbol{\varepsilon}}{\partial x}d\Omega = \frac{1}{A_k^s}\int_{\Gamma_k^s}\boldsymbol{\varepsilon}\mathbf{n}_x d\Gamma \\ \boldsymbol{\varepsilon}_{ky}^{'} &= \frac{1}{A_k^s}\int_{\Omega_k^s}\frac{\partial \boldsymbol{\varepsilon}}{\partial y}d\Omega = \frac{1}{A_k^s}\int_{\Gamma_k^s}\boldsymbol{\varepsilon}\mathbf{n}_y d\Gamma \end{aligned} \tag{18}$$

For the *x* direction,

$$\boldsymbol{\varepsilon}'_{kx}=\frac{1}{A_k^s}\int_{\Omega_k^s}\frac{\partial\boldsymbol{\varepsilon}}{\partial x}d\Omega=\frac{1}{A_k^s}\int_{\Gamma_k^s}\boldsymbol{\varepsilon}n_x d\Gamma=\frac{1}{A_k^s}\int_{\Gamma_k^s}\mathbf{B}\mathbf{u}n_x d\Gamma=\frac{1}{A_k^s}\sum_{i=1}^{N}\int_{\Gamma_k^s}\mathbf{B}_I\mathbf{u}_I n_x d\Gamma$$

$$\frac{\partial\tilde{\mathbf{B}}}{\partial x}=\frac{1}{A_k^s}\int_{\Gamma_k^s}\mathbf{B}_I n_x d\Gamma=\frac{1}{A_k^s}\int_{\Gamma_k^s}\begin{bmatrix}\frac{\partial N_I}{\partial x} & 0\\ 0 & \frac{\partial N_I}{\partial y}\\ \frac{\partial N_I}{\partial y} & \frac{\partial N_I}{\partial x}\end{bmatrix}n_x d\Gamma \text{ with } \begin{cases}\int_{\Gamma_k^s}\frac{\partial N_I}{\partial x}n_x d\Gamma=\sum_{seg=1}^{M}\frac{\partial N_I(x_{seg}^{GP})}{\partial x}n_{x,seg}l_{seg}\\ \int_{\Gamma_k^s}\frac{\partial N_I}{\partial y}n_x d\Gamma=\sum_{seg=1}^{M}\frac{\partial N_I(x_{seg}^{GP})}{\partial y}n_{x,seg}l_{seg}\end{cases} \quad (19)$$

Similarly, for the *y* direction,

$$\boldsymbol{\varepsilon}'_{ky}=\frac{1}{A_k^s}\int_{\Omega_k^s}\frac{\partial\boldsymbol{\varepsilon}}{\partial y}d\Omega=\frac{1}{A_k^s}\int_{\Gamma_k^s}\boldsymbol{\varepsilon}n_y d\Gamma=\frac{1}{A_k^s}\int_{\Gamma_k^s}\mathbf{B}\mathbf{u}n_y d\Gamma=\frac{1}{A_k^s}\sum_{i=1}^{N}\int_{\Gamma_k^s}\mathbf{B}_I\mathbf{u}_I n_y d\Gamma$$

$$\frac{\partial\tilde{\mathbf{B}}}{\partial y}=\frac{1}{A_k^s}\int_{\Gamma_k^s}\mathbf{B}_I n_y d\Gamma=\frac{1}{A_k^s}\int_{\Gamma_k^s}\begin{bmatrix}\frac{\partial N_I}{\partial x} & 0\\ 0 & \frac{\partial N_I}{\partial y}\\ \frac{\partial N_I}{\partial y} & \frac{\partial N_I}{\partial x}\end{bmatrix}n_y d\Gamma \text{ with } \begin{cases}\int_{\Gamma_k^s}\frac{\partial N_I}{\partial x}n_y d\Gamma=\sum_{seg=1}^{M}\frac{\partial N_I(x_{seg}^{GP})}{\partial x}n_{y,seg}l_{seg}\\ \int_{\Gamma_k^s}\frac{\partial N_I}{\partial y}n_y d\Gamma=\sum_{seg=1}^{M}\frac{\partial N_I(x_{seg}^{GP})}{\partial y}n_{y,seg}l_{seg}\end{cases} \quad (20)$$

For the four subdomains, the strain can be expressed as

$$\begin{aligned}\boldsymbol{\varepsilon}_1^{sc}&=\boldsymbol{\varepsilon}_I-\boldsymbol{\varepsilon}'_{kx}l_c,\ \boldsymbol{\varepsilon}_2^{sc}=\boldsymbol{\varepsilon}_I-\boldsymbol{\varepsilon}'_{ky}l_c\\ \boldsymbol{\varepsilon}_3^{sc}&=\boldsymbol{\varepsilon}_I+\boldsymbol{\varepsilon}'_{kx}l_c,\ \boldsymbol{\varepsilon}_4^{sc}=\boldsymbol{\varepsilon}_I+\boldsymbol{\varepsilon}'_{ky}l_c\end{aligned} \quad (21)$$

Finally, the internal force vectors can be expressed as

$$\mathbf{F}_{\text{stable}}^{\text{int}}=\int_\Omega\tilde{\mathbf{B}}^{\mathrm{T}}\cdot\bar{\boldsymbol{\sigma}}\,d\Omega+\int_\Omega l_c\cdot\left(\frac{\partial\tilde{\mathbf{B}}}{\partial x}^{\mathrm{T}}\cdot\Delta\bar{\boldsymbol{\sigma}}_x+\frac{\partial\tilde{\mathbf{B}}}{\partial y}^{\mathrm{T}}\cdot\Delta\bar{\boldsymbol{\sigma}}_y\right)d\Omega \quad (22)$$

where $\bar{\boldsymbol{\sigma}}=\frac{\left(\boldsymbol{\sigma}_1^{sc}+\boldsymbol{\sigma}_2^{sc}+\boldsymbol{\sigma}_3^{sc}+\boldsymbol{\sigma}_4^{sc}\right)}{4}$ is the mean stress for four subdomains, $\Delta\bar{\boldsymbol{\sigma}}_x=\frac{\boldsymbol{\sigma}_3^{sc}-\boldsymbol{\sigma}_1^{sc}}{2}$ the mean stress increment along the *x*-axis, and $\Delta\bar{\boldsymbol{\sigma}}_y=\frac{\boldsymbol{\sigma}_4^{sc}-\boldsymbol{\sigma}_2^{sc}}{2}$ the mean stress increment along the *y*-axis. The global stiffness matrix around node *k* can be calculated following Eq.(14) for 2D solid mechanics problems:

$$\mathbf{K}=\sum_{k=1}^{N_n}\left(\tilde{\mathbf{B}}_{\mathrm{k}}{}^{\mathrm{T}}\mathbf{D}\tilde{\mathbf{B}}_{\mathrm{k}}A_{\mathrm{k}}^{s}+\left(\frac{\partial\tilde{\mathbf{B}}}{\partial x}\right)_{k}^{T}\mathbf{D}\left(\frac{\partial\tilde{\mathbf{B}}}{\partial x}\right)_{k}\frac{A_{k}^{s}}{2}+\left(\frac{\partial\tilde{\mathbf{B}}}{\partial y}\right)_{k}^{T}\mathbf{D}\left(\frac{\partial\tilde{\mathbf{B}}}{\partial y}\right)_{k}\frac{A_{k}^{s}}{2}\right) \tag{23}$$

Compared to NS-PFEM, the strain in smoothing domain is linear other than constant. Regarding to the calculation of internal force, a stabilization term contributed by the stress difference in smoothing domain is added. The stiffness matrix is also the same situation. It is worth mentioning that the four supplementary integration points are not actual integration points but just temporary variables to better capture the stress distribution, which is accomplished equivalently by one point integration and the stabilization terms [36].

The core idea of the presented stabilization technique is similar to SNS-FEM in [26, 36] and the naturally stabilized nodal integration (NSNI) in Galerkin meshfree method [37]. All these methods use the gradients of strains at nodes to stabilize the direct nodal integration. In this study, the gradient of $\tilde{\mathbf{B}}$ is calculated using the first derivatives of the shape function different from the smoothed derivatives of shape function in SNS-FEM [26, 36]. Compared to NSNI that mainly uses the stabilization of reproducing kernel particle method (RKPM) [37], the stabilization in the proposed SNS-PFEM uses triangular element to construct the nodal integration area and the linear interpolation function in T3 element, which is an extension of the NSNI with better conciseness and computational efficiency.

2.3 Time discretisation and computational cycle of SNS-PFEM

The central difference time integration scheme in combination with the computational cycle used in the proposed SNS-PFEM is summarised as:

1. *Initialization of geometry, parameters of soil model.*
2. *Discretize the domain into a set of nodes/particles.*
3. *Build the computational mesh using the Delaunay triangulation technique.*
4. *Define the domain boundary using an alpha shape method.*
5. *Step into time integration, initializing velocity and acceleration*
   - *5.1 Update velocity at mid time step*
   - *5.2 Calculate the smoothed B matrix via Eq.(12) and its gradients via Eqs.(19) and (20)*
   - *5.3 Get the increment of displacement and then the strain increment via Eq.(21).*
   - *5.4 Calculate the stress increment of four virtual supplementary gauss points via constitutive law and update effective stress (Eq.(5))*

5.5 Calculate the internal force via Eq.(22).

6. *Solve the governing equation via Eq.(9)*
7. *Update the accelerations.*
8. *Update velocity at this time step.*
9. *Check the mesh quality. If ok, go to step 5.1, otherwise perform the remeshing by Delaunay triangulation and alpha shape (step 3-step 4)and then go to step 5.1*
10. *Until the loading time.*

3 Numerical validations for the SNS-PFEM

In this section, two kinds of tests are simulated for validation: (a) using two benchmark tests (i.e. cantilever beam and infinite plate with a circular hole) on elastic material to examine the convergence and accuracy of SNS-PFEM; (b) using three representative elastoplastic tests (i.e. cavity expansion, penetration of a rigid footing and progressive landslide) to examine the performance of SNS-PFEM on solving large deformation in terms of accuracy and temporal instability. All calculations were made on a desktop computer with an Intel Core i9-9900K running at 3.60 GHz, with 64 GB of RAM. Note that the cases on elastic material have been commonly used for testing the convergence and accuracy of NS-FEM and SNS-FEM [20, 26, 27, 36, 40]. In this study, such cases are simply simulated and some results are just reproduced. In contrast, the cases on elastoplastic material related to geotechnical engineering are paid more attention.

3.1 Cantilever beam

The cantilever beam case is a regular benchmark for various numerical methods to test the convergence performance [25-27, 36]. Fig. 3 shows a cantilever beam with length L and height H under a parabolic traction on the free boundary.

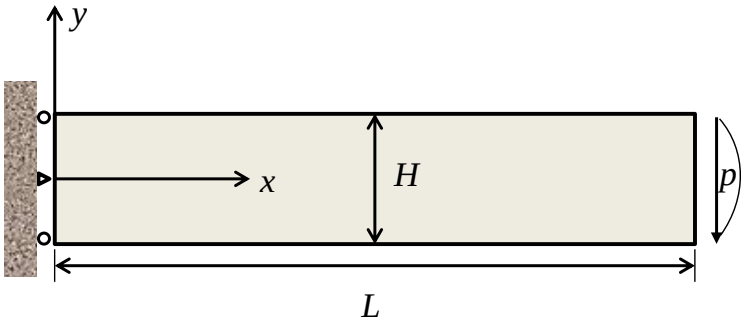

Fig. 3 Cantilever beam subjected to a parabolic traction on the free edge

The beam is assumed to be a unit thickness. The analytical solution of displacement in both directions can be expressed by Eq.(24).

$$\begin{cases} u_x(x,y) = \dfrac{Py}{6EI}\left[(6L-3x)x+(2+v)\left(y^2-\dfrac{H^2}{4}\right)\right] \\ u_y(x,y) = -\dfrac{P}{6EI}\left[3vy^2(L-x)+(4+5v)\dfrac{H^2x}{4}+(3L-x)x^2\right] \end{cases} \tag{24}$$

where $I = H^3/12$ is the moment of inertia for the beam. The solution of stresses is as follows

$$\sigma_{xx}(x,y) = \frac{Py}{I}(L-x), \sigma_{yy}(x,y) = 0, \tau_{xy}(x,y) = -\frac{P}{2I}\left(\frac{H^2}{4}-y^2\right) \tag{25}$$

In this case, L is set to 48 m and H is set to 12 m. The material is elastic with the following parameters: Young's modulus $E = 3.0 \times 10^4$ N/m^2, Poisson's ratio $\upsilon = 0.3$. The loading pressure is $P = 1 \times 10^3$ N. The domain is discretized into 85 particles, and the number of elements is 128. In order to demonstrate the performance of the proposed SNS-PFEM with stabilization, the original methods T3-PFEM (PFEM using T3 element) and NS-PFEM are also adopted to simulate the same case for comparisons. Fig. 4 presents the simulated displacements with corresponding relative errors compared to the analytical solution produced by T3-PFEM, NS-PFEM and the proposed SNS-PFEM. It can be found that the T3-PFEM is stiffer than SNS-PFEM, the NS-PFEM is softer than SNS-PFEM, and the SNS-PFEM is closest to the exact solution. Fig. 5 shows the distribution of the shear stress along the section of $x = L/2$. The performance of SNS-PFEM is better than other two methods comparing to the analytical solution. Fig. 6 presents the comparison of strain energy solutions for three methods. It can be observed that the NS-PFEM possesses the upper bound property and the SNS-PFEM is much better than the NS-PFEM and T3-PFEM.

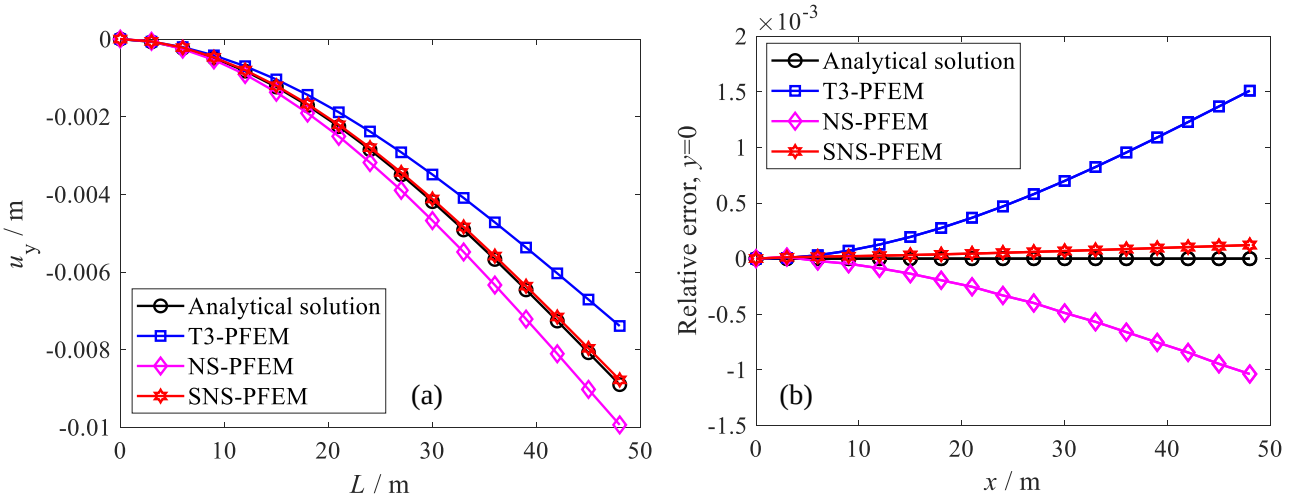

Fig. 4 (a) Distribution of vertical displacements along (x, 0) and (b) relative errors of vertical displacement for the cantilever under a parabolic traction at the free edge

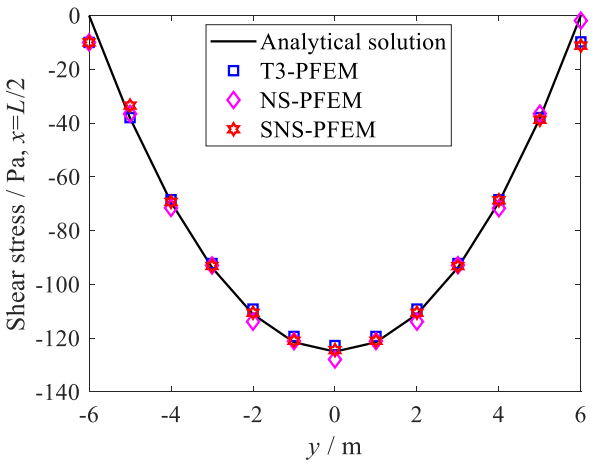

Fig. 5 Distribution of the shear stress along the section of $x = L/2$ in the cantilever under a parabolic traction at the free edge

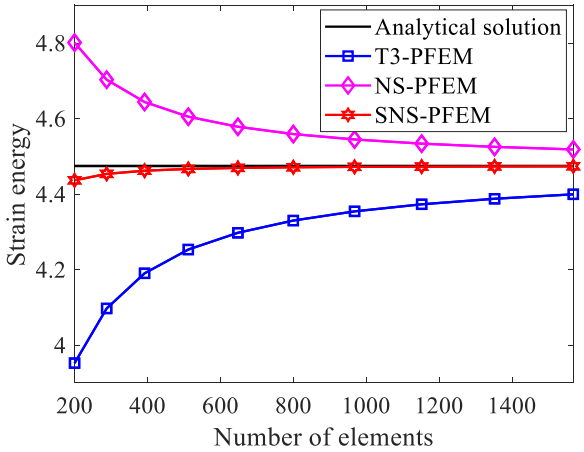

Fig. 6 Comparison of strain energy solutions for the cantilever under a parabolic traction at the free edge

3.2 Infinite plate with a circular hole

In this section, an infinite plate with a central circular hole of radius r=1 subjected to a unidirectional tensile load of p=1.0 N/m^2 is simulated. Due to the symmetry, only the upper right quarter is modelled (b=5 m), as shown in Fig. 7. The domain is discretised into 734 particles, and the initial number of elements is 1368. The material is elastic with following parameters: Young's modulus E = 1.0 × 10^3 N/m^2 and Poisson's ratio υ = 0.3.

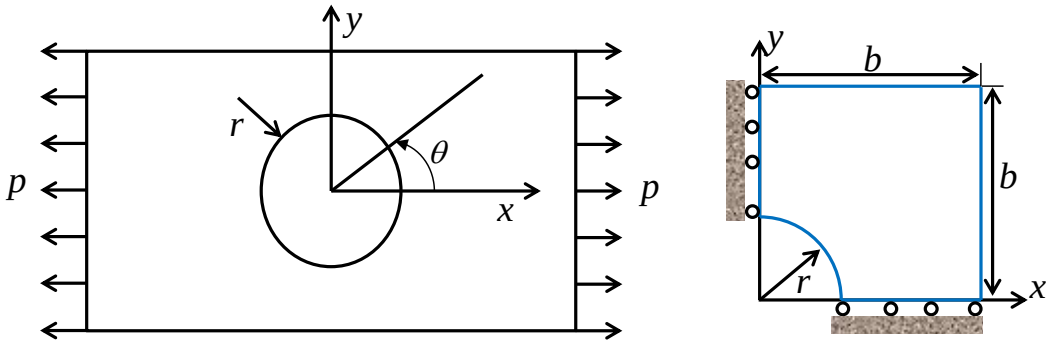

Fig. 7 Infinite plate with a circular hole subjected to unidirectional tension

The analytical solutions for stresses and displacements are presented as follows:

$$\begin{cases} \sigma_x = 1-\dfrac{a^2}{r^2}\left[\dfrac{3}{2}\cos 2\theta+\cos 4\theta\right]+\dfrac{3a^4}{2r^4}\cos 4\theta \\ \sigma_y = -\dfrac{a^2}{r^2}\left[\dfrac{1}{2}\cos 2\theta-\cos 4\theta\right]-\dfrac{3a^4}{2r^4}\cos 4\theta \\ \tau_{xy} = -\dfrac{a^2}{r^2}\left[\dfrac{1}{2}\sin 2\theta+\sin 4\theta\right]+\dfrac{3a^4}{2r^4}\sin 4\theta \end{cases} \tag{26}$$

$$\begin{cases} u_x = \dfrac{a}{8\mu}\left[\dfrac{r}{a}(\kappa+1)\cos\theta+2\dfrac{a}{r}((1+\kappa)\cos\theta+\cos 3\theta)-2\dfrac{a^3}{r^3}\cos 3\theta\right] \\ u_y = \dfrac{a}{8\mu}\left[\dfrac{r}{a}(\kappa-1)\sin\theta+2\dfrac{a}{r}((1-\kappa)\sin\theta+\sin 3\theta)-2\dfrac{a^3}{r^3}\sin 3\theta\right] \end{cases} \tag{27}$$

where $\mu = E/(2(1+\upsilon))$, κ is defined in terms of Poisson's ratio by $\kappa = 3-4\upsilon$ for plane strain cases.

where $\mu = E/(2(1+\upsilon))$, κ is defined by $\kappa = 3-4\upsilon$ for plane strain cases.

Fig. 8 presents the results of normal stresses along the left and bottom boundaries, respectively. Fig. 9 shows the displacements along these boundaries. The numerical results of SNS-PFEM for displacements and normal stresses are found in good agreement with the analytical solutions. Fig. 10 presents the comparison of strain energy for three methods, which shows that the SNS-PFEM converges to the analytical solution better than the NS-PFEM and T3-PFEM. All results demonstrate that the linear smoothed strain field function (SNS-PFEM) is more stable and performs better than the constant smoothed strain function (NS-PFEM).

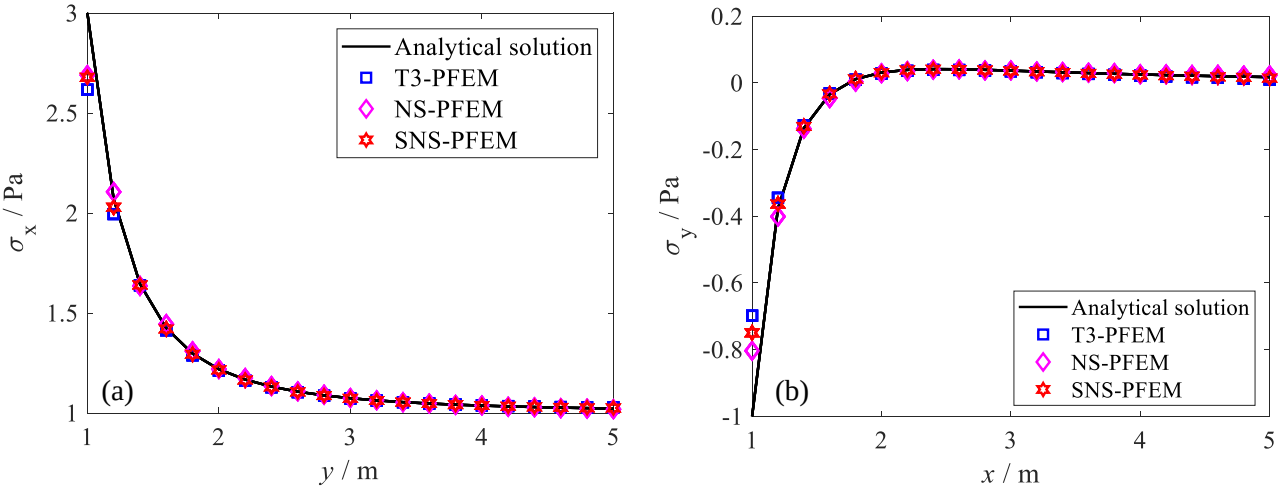

Fig. 8 Distribution of normal stress: (a) along the left boundary and (b) along the bottom boundary, of the infinite plate with a hole subjected to unidirectional tension

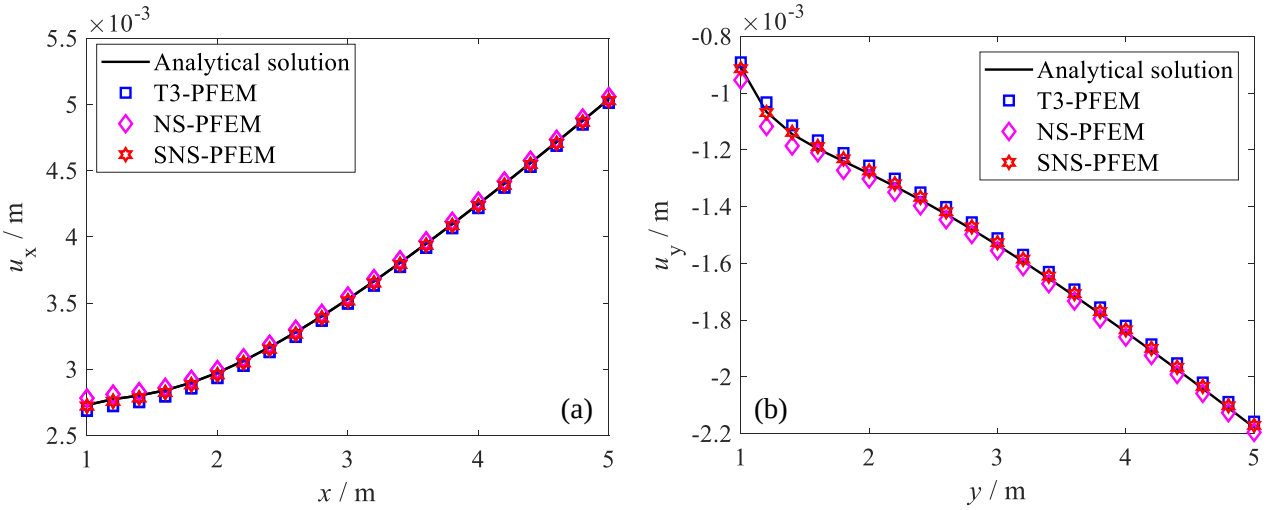

Fig. 9 Distribution of displacement: (a) along the bottom boundary and (b) along the left boundary, of the infinite plate with a hole subjected to unidirectional tension

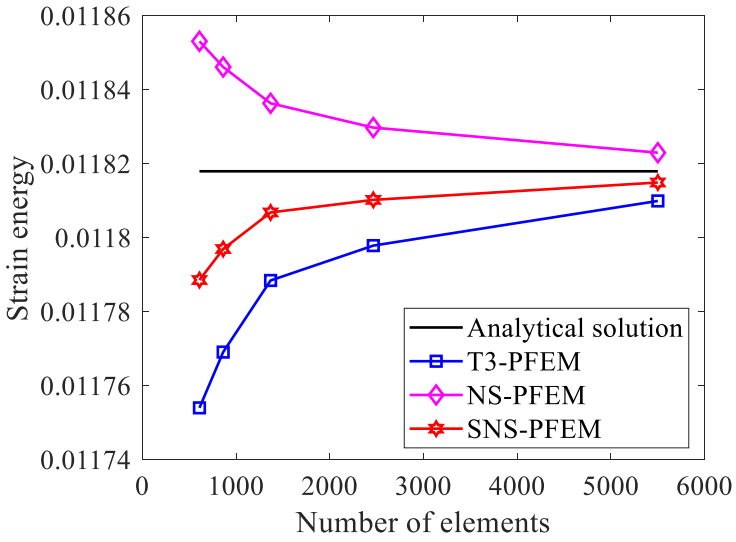

Fig. 10 Strain energy of the infinite plate with a hole subjected to unidirectional tension

3.3 Cavity expansion

In this case, the expansion of a long cylindrical cavity in infinite undrained soil mass is simulated. Since the problem involves the material and geometric nonlinearities, it is a suitable benchmark to validate the SNS-PFEM. An analytical solution for this problem has been proposed by Yu [41], which can be used to examine the accuracy of SNS-PFEM on elastoplastic material.

Due to the symmetry, only 1/4 of the problem is simulated. A plane strain condition is assumed. Fig. 11 shows the geometry, mesh and boundary of the cavity expansion problem. To eliminate the boundary effect for the infinite mass, the geometry can be as large as possible under the premise of not affecting the calculation efficiency and accuracy. The domain is discretised into 1199 particles, and the number of elements is 2278. The initial internal pressure is set to p_0 (=0 in this case). The initial internal radius is a_0 and the current radius is a. The analytical solution of internal pressure p by Yu [41] is presented as:

$$\frac{p-p_0}{s_u}=1+\ln\left[\frac{G}{s_u}\left(1-\left(\frac{a_0}{a}\right)^2\right)+\left(\frac{a_0}{a}\right)^2\right] \tag{28}$$

where G is shear modulus and s_u is the undrained shear strength. It is the special case of a cylindrical cavity in an infinite incompressible undrained clay.

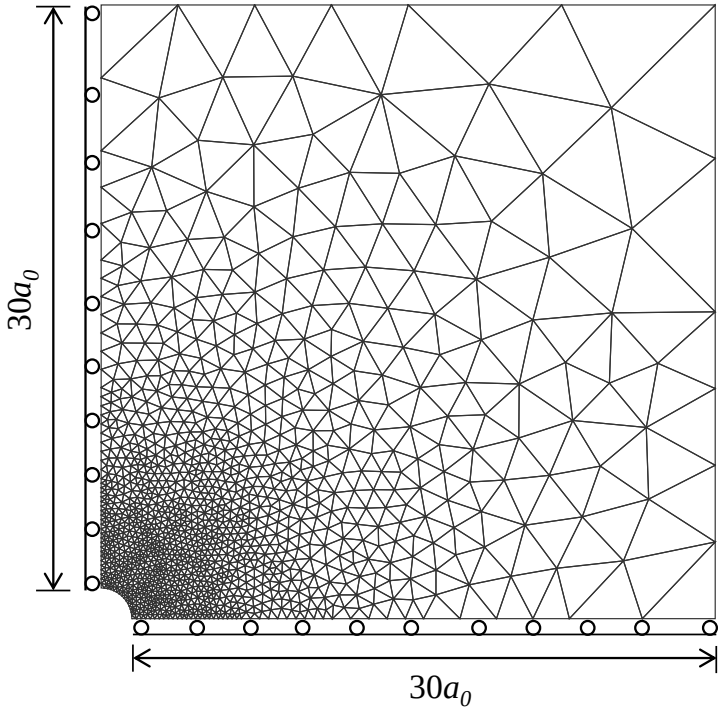

Fig. 11 Geometry and mesh of cavity expansion in Tresca soil

In the simulation, the expansion speed is set to 0.01 m/s. A final expansion distance of 1.5 m (1.5a) is simulated. The elastic–perfectly plastic Tresca model with following parameters: Young's modulus E=461.5 kPa, Poisson's ratio υ=0.499 and undrained shear strength s_u=8.66 kPa, is adopted for simulating the behaviour of undrained clay. The time step is set to 5×10^{-5} s.

Fig. 12 shows the results of normalized internal pressure q/s_u versus normalized radial displacement a/a_0 using SNS-PFEM and NS-PFEM compared to the analytical solution. The NS-PFEM and SNS-PFEM can give a reasonable prediction when the deformation is small (a<0.5a_0). With the increase of expansion displacement, the SNS-PFEM can still give the "close-to-exact" solution while the NS-PFEM becomes unstable and produces less accurate prediction due to the temporal instability, which can be found and explained by the distribution of radial stress at different expansion distance for both SNS-PFEM and NS-PFEM in Fig. 13. In other words, the temporal instability of NS-PFEM can be cured by the adopted stabilization technique considering the strain gradient in the smoothing domain in SNS-PFEM. Note that the case in Zhang et al. [14] was simulated by the implicit NS-PFEM, it is considered as a static problem. Since the temporal instability does not influence the calculation of the static problem, the implicit NS-PFEM simulation

is stable. However, the temporal instability affects the dynamic analysis, that's why, when the case of Zhang et al. [14] is simulated by the explicit NS-PFEM with time integration, the results become unstable.

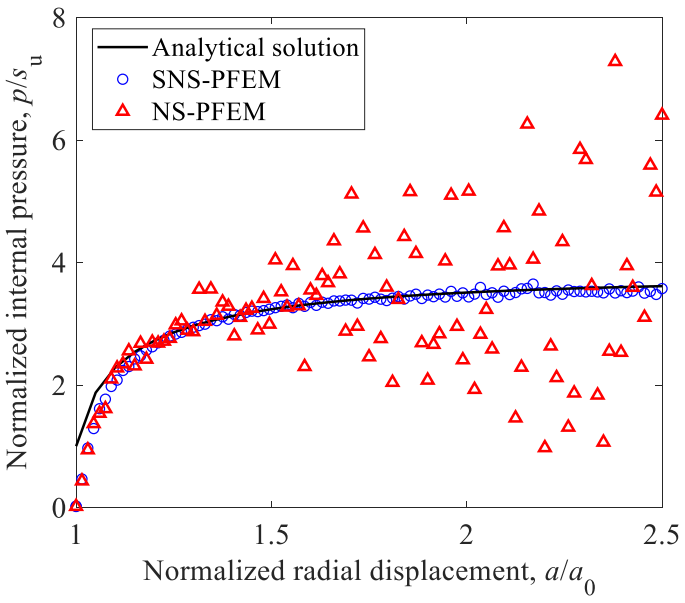

Fig. 12 Normalized internal pressure q/s_u versus normalized radial displacement a/a_0

a/a_0	NS-PFEM	SNS-PFEM
1.25	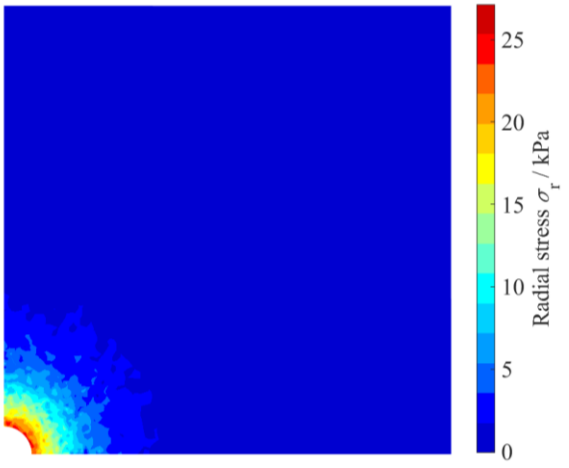	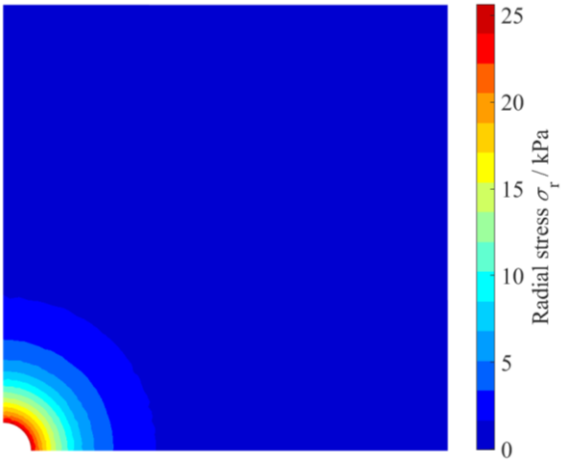

1.5	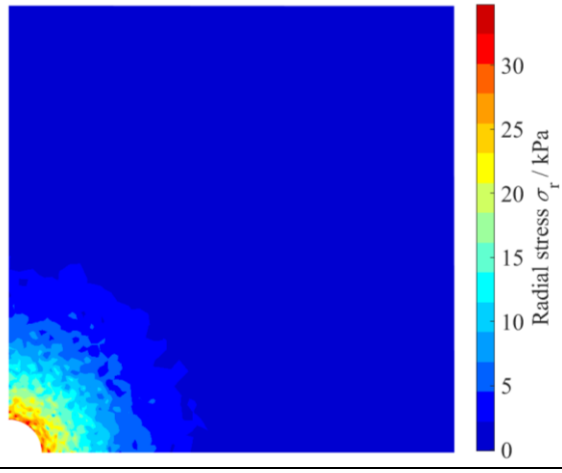 Radial stress σ_r / kPa 0 5 10 15 20 25 30	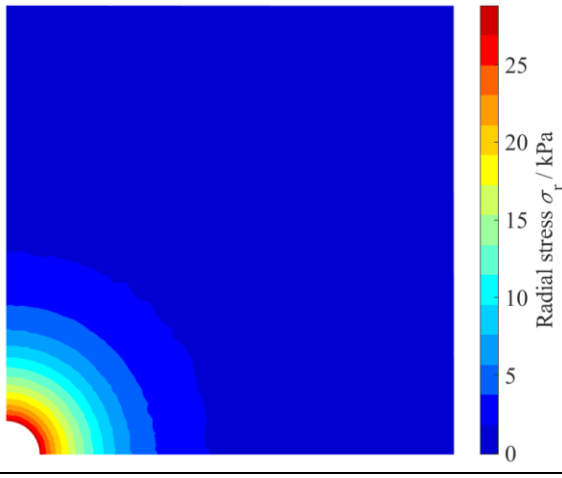 Radial stress σ_r / kPa 0 5 10 15 20 25
1.75	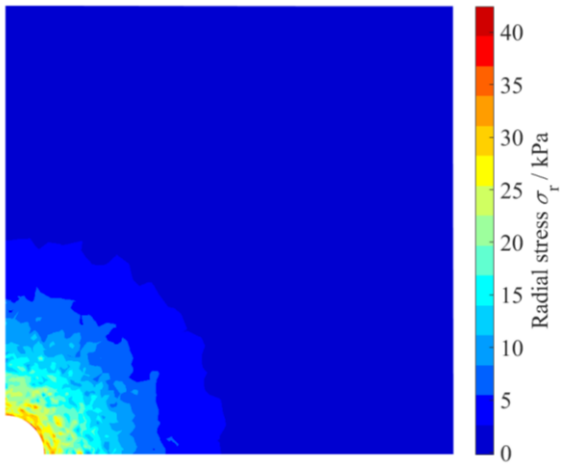 Radial stress σ_r / kPa 0 5 10 15 20 25 30 35 40	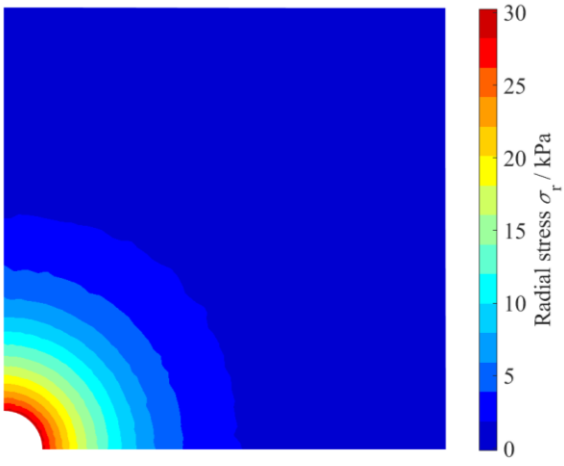 Radial stress σ_r / kPa 0 5 10 15 20 25 30
2.0	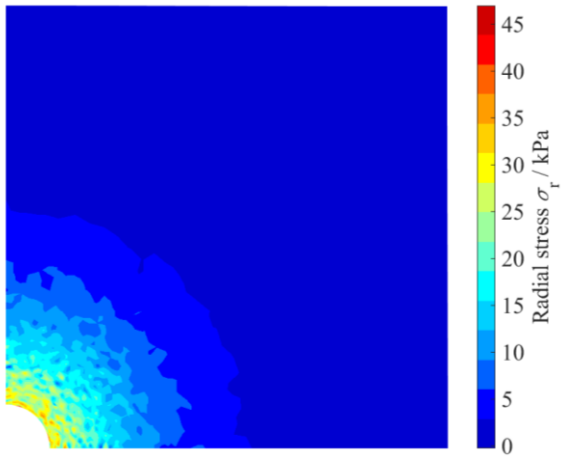 Radial stress σ_r / kPa 0 5 10 15 20 25 30 35 40 45	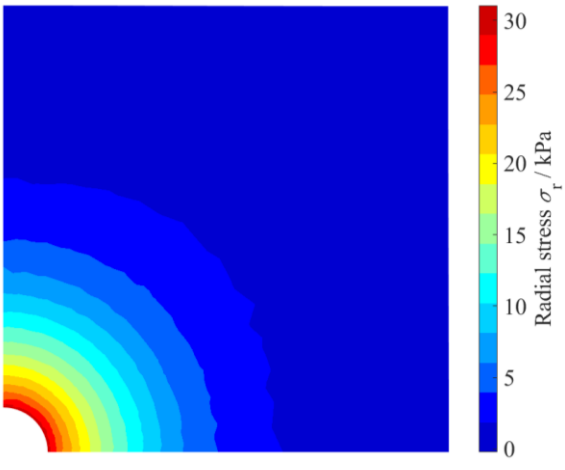 Radial stress σ_r / kPa 0 5 10 15 20 25 30

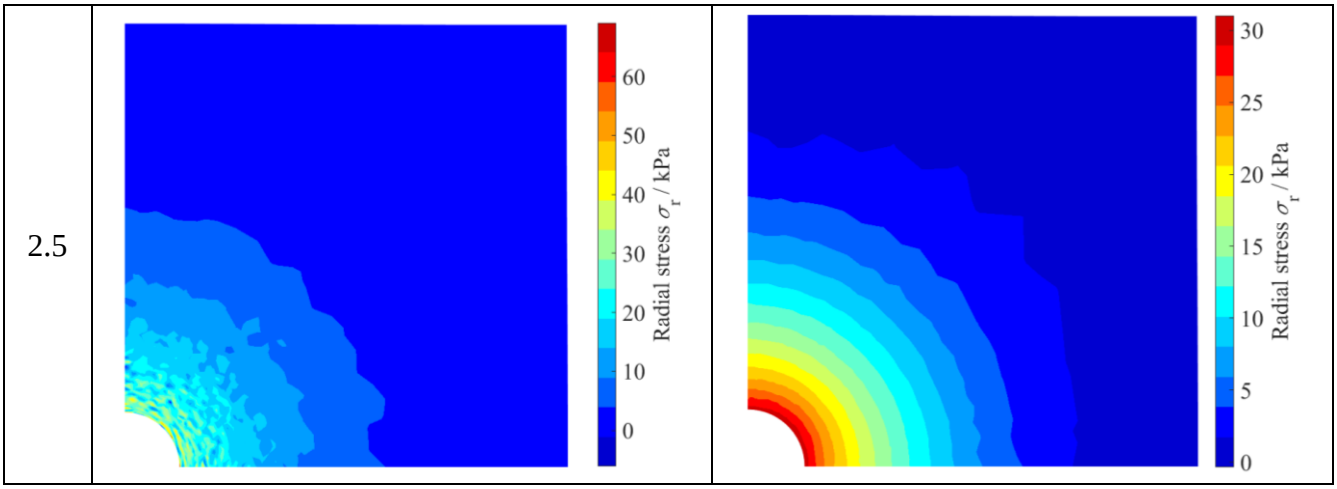

Fig. 13 Distribution of radial stress σ_r of the cavity expansion problem at different radial displacements

3.4 Penetration of a rigid footing in soft soil

This case has already been simulated using the PFEM with T6 element [42], MPM [43], FEM-ALE [44], NS-PFEM [12, 14] and ES-PFEM [18]. A comparison of the results of the proposed SNS-PFEM and those of the other solutions can demonstrate the accuracy of the SNS-PFEM. Fig. 14 shows the geometry and mesh of the footing problem. The width of strip foundation B is assumed to be 2.0 m, with width and depth of 5B, to reduce the boundary effect. A plane strain condition for the simulation is assumed. The bottom side is fixed in the horizontal and vertical directions, whereas the right-hand side is fixed in only the horizontal direction. To improve computational efficiency, a non-uniform mesh is examined. The domain is discretised into 4469 particles, and the initial number of elements is 8743. The mesh is dense enough to obtain accurate results, according to the investigations of Yuan et al. [13].

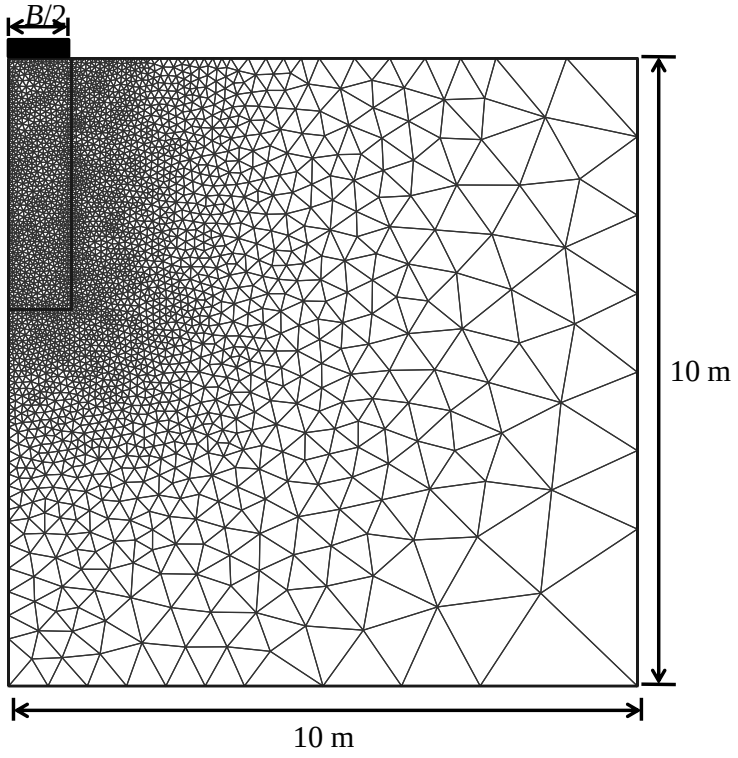

Fig. 14 Geometry and mesh of the footing problem

In the simulation, the penetration speed of the footing is set to 0.01 m/s. A final penetration depth of 2.0 m (= B) is simulated to allow fair comparison with other simulations [6, 45, 46]. The initial time step is 0.001. The time step is dynamically adjusted depending on the mesh quality during the calculation. The soil behaviour is described by the elastic–perfectly plastic Tresca model, reduced from the MC model with friction angle=0°. To allow comparison with analytical solutions, the following parameters are adopted: Young's modulus E=100 kPa, Poisson's ratio υ=0.495 and undrained shear strength c_u=1 kPa. Note that volumetric locking is the over stiffening of elements when the material is close to being incompressible (Poisson's ratio nearing 0.5). This stiffening happens when a fully integrated element is used. To show the performance of SNS-PFEM on solving volumetric locking problem, the footing case was also simulated by T3-PFEM.

Fig. 15 shows a comparison of the results in terms of a normalised vertical reaction force versus penetration depth between the SNS-PFEM and other solutions (including two reference solutions $(\pi+2)c_u = 5.14c_u$ of Prandtl [47] and $(2\pi+2)c_u = 8.28c_u$ of Meyerhof [48]). Note that the results computed by the SNS-PFEM are obtained under large deformation conditions and exceed the

plasticity solution of Prandtl. If the small deformation condition is considered, it is interesting that the obtained solution by SNS-PFEM is very close to the plasticity solution of Prandtl, which reveals the expectation of a steady plastic flow and steady bearing capacity for the footing. It can be clearly seen that all results except the T3-PFEM are located between the analytical solution obtained by Prandtl [47] and the limit load obtained by Meyerhof [48], demonstrating the accuracy of the SNS-PFEM. Without special treatment, the T3-PFEM gives a large bearing capacity, demonstrating the occurrence of volumetric locking for T3 element. Whilst, using the same T3 element, the SNS-PFEM and NS-PFEM can give more reasonable solutions, which indicates that the proposed SNS-PFEM, like the NS-PFEM, can avoid volumetric locking when using the T3 element. Moreover, the obtained curve of SNS-PFEM is closer to the solutions obtained by the T6-PFEM [42], MPM [43] and FEM-ALE [44] but higher than that obtained by the NS-PFEM [12, 14]. That, in turn, indicates that the stabilisation technique taking into account the strain gradient in the smooth domain can effectively solve the 'overly soft' problem of the NS-PFEM. The proposed SNS-PFEM has a close-to-exact stiffness and often offers super-convergent and very accurate solutions compared with those offered by the traditional NS-PFEM. Furthermore, for the same mesh (Fig. 14), the CPU time for the SNS-PFEM simulation is 5h 13min owing to the addition of a few more integration points, whereas for the NS-PFEM simulation it is 3h 51min. The efficiency of the SNS-PFEM is also acceptable.

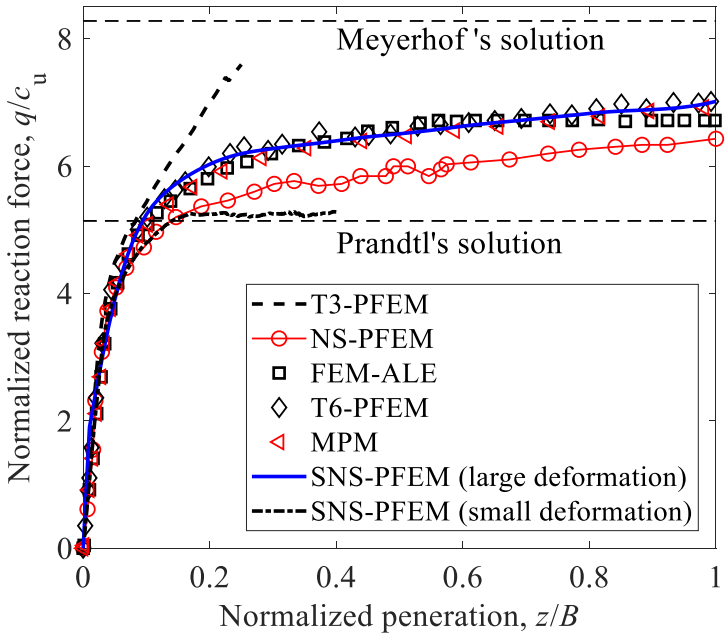

Fig. 15 Normalised reaction force–displacement curves from footing penetration analysis of Tresca soil and compared with other solutions

Apart from the curve of bearing capacity, the contours of some variables also reflect the enhanced performance of the proposed SNS-PFEM. Due to overly soft problem of NS-PFEM, the temporal instability can be easily triggered in large deformation problem. The result of NS-PFEM usually exhibits discontinuous and point shape distribution, which reflects the temporal instability [36]. Accordingly, the smoothness of contour can be served as evidence to highlight the performance of the implementation of stabilization. Fig. 16 compares the contours for equivalent plastic strain (PEEQ) $\varepsilon_{\mathrm{eq}}^{p}=\sqrt{2\left(\boldsymbol{\varepsilon}^{p}:\boldsymbol{\varepsilon}^{p}\right)/3}$ ($\boldsymbol{\varepsilon}^{p}$ is the plastic strain tensor), shear stress σ_{xy} and mean stress p obtained by the NS-PFEM and SNS-PFEM. It is clearly seen that the contours of PEEQ, σ_{xy} and p for the SNS-PFEM are more continuous and smoother than that for the NS-PFEM. In SNS-PFEM, the overly-soft behavior of NS-PFEM is significantly solved by adding a stabilisation term into internal force, which implies the improvement of eigenvalues of stiffness matrix in contrast to mass matrix and hence the temporal instability (i.e., non-zero-energy spurious modes) can be avoided.

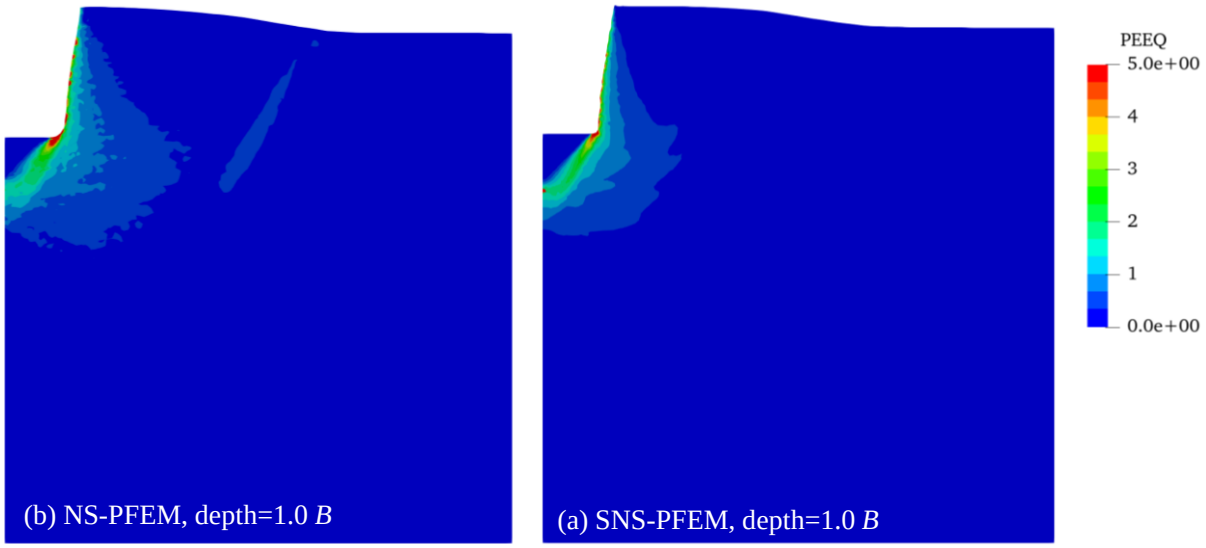

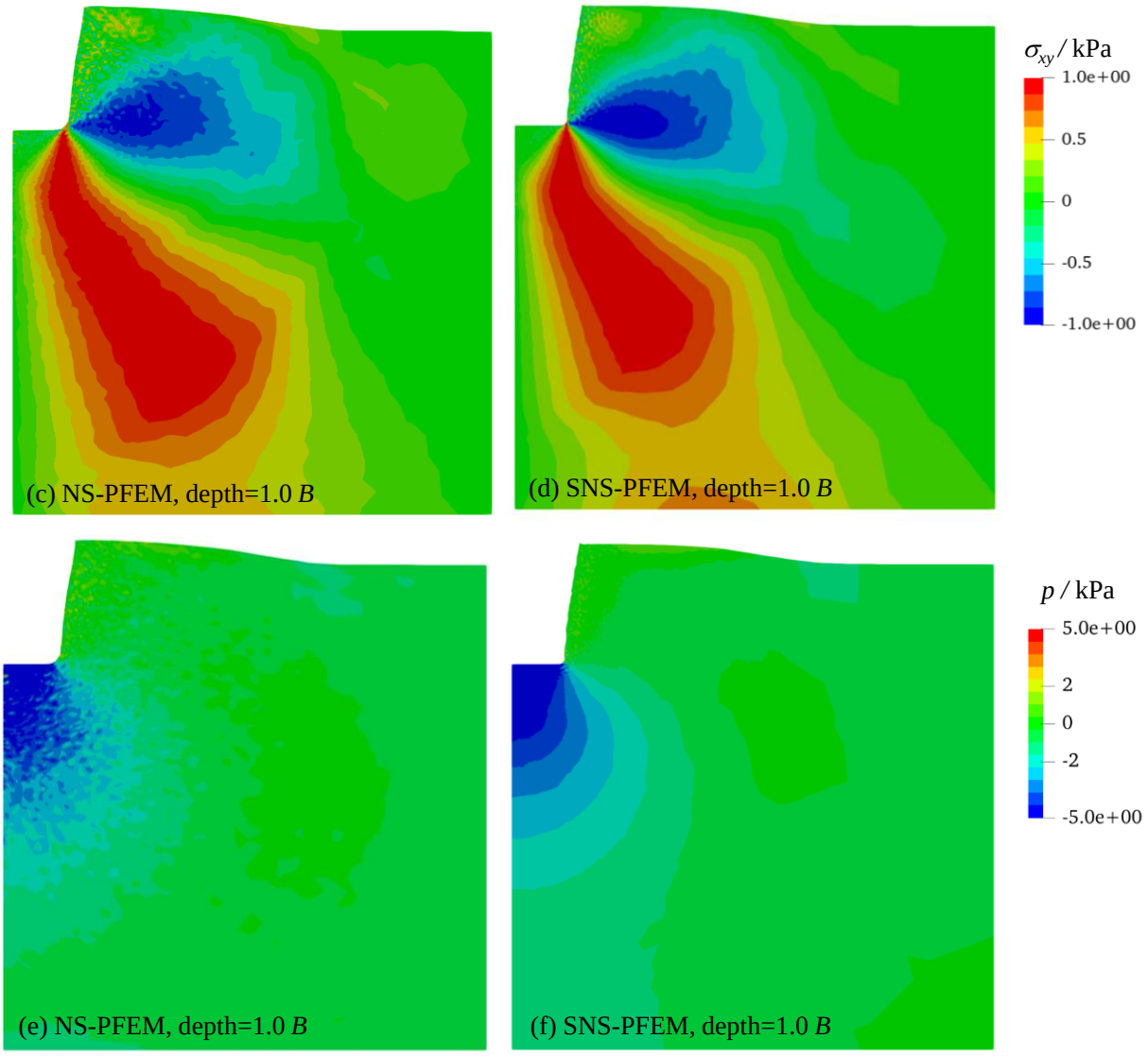

Fig. 16 Contour of equivalent plastic strain, shear stress and mean stress at a penetration depth of 2 m

It can be found that the presented bearing capacity curve and contours are closer to the results calculated by the ES-PFEM [18], which can offer super-convergent and highly accurate solutions. Thus all results demonstrate that the introduction of the stabilisation term gives the SNS-PFEM a 'close to exact' stiffness, thereby solving the 'overly soft' problem associated with the NS-PFEM.

3.5 Progressive landslide

To demonstrate the outstanding performance of the proposed SNS-PFEM, the progressive failure of slope of sensitive clay is simulated. Fig. 17 shows the geometric configuration of a sensitive clay deposit. The domain is discretised into a total of 6169 particles (11925 3-node triangular elements). According to [12, 15, 17, 18, 49], a soil model that takes strain softening into

account is necessary for reproducing the progressive failure. To well simulate such progressive landslides, the Mohr-Coulomb model that takes strain softening into account, as proposed by Yerro et al. [50], is adopted. The softening behaviour is achieved by reducing the effective strength parameters (friction angle ϕ and cohesion c) with the accumulated equivalent plastic strain $\varepsilon_{\mathrm{eq}}^{p}$ according to the exponential softening rules

$$\begin{cases} c = c_r + \left(c_p - c_r\right) e^{-\eta \varepsilon_{\mathrm{eq}}^{p}} \\ \phi = \phi_r + \left(\phi_p - \phi_r\right) e^{-\eta \varepsilon_{\mathrm{eq}}^{p}} \end{cases} \tag{29}$$

where the subscripts $_r$ and $_p$ represent the residual and peak values, respectively, and η is the shape factor used to control the rate of degradation.

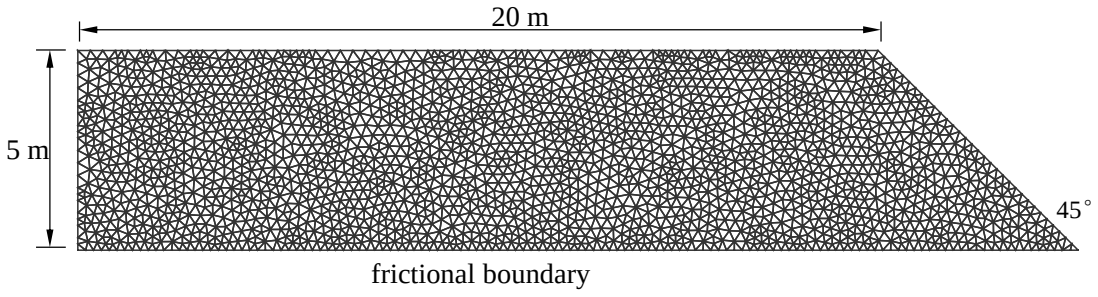

Fig. 17 Geometry of a homogeneous soil slope

Following previous simulations by Jin et al [17, 18], the following parameters are adopted in the simulation: Young's modulus E=1×10^3 kPa; friction angle ϕ=0°, assuming undrained shear strength totally taking by the cohesion; dilatancy angle ψ=0°; peak cohesion c_{p}=20 kPa; residual cohesion c_{r}=4.0 kPa; and shape factor η=4, which is approximately equivalent to the value used by Yuan et al. [12]. Note that, the MC model with strain softening can't totally represent the behaviour of sensitive clay, such as anisotropy, creep and destructuration [51, 52]. Since the strain softening is the most important feature of sensitive clay for the case of progressive landslide [49, 53, 54], the MC model with strain softening is adopted for the simplicity. Such model has also been widely adopted in simulating progressive landslides in the community [12, 17]. The soil density is ρ=1.7×10^3 kg/m^3. To achieve an approximate undrained condition, the Poisson's ratio υ is set to 0.49 [12, 17, 18]. The frictional coefficient μ between the sensitive clay and the rigid bottom surface is set to 0.3, consistent

with the value used by Yuan et al [12]. The initial stress was generated by gravity loading with the earth pressure coefficient K_0=0.5. The initial time step is 0.0003.

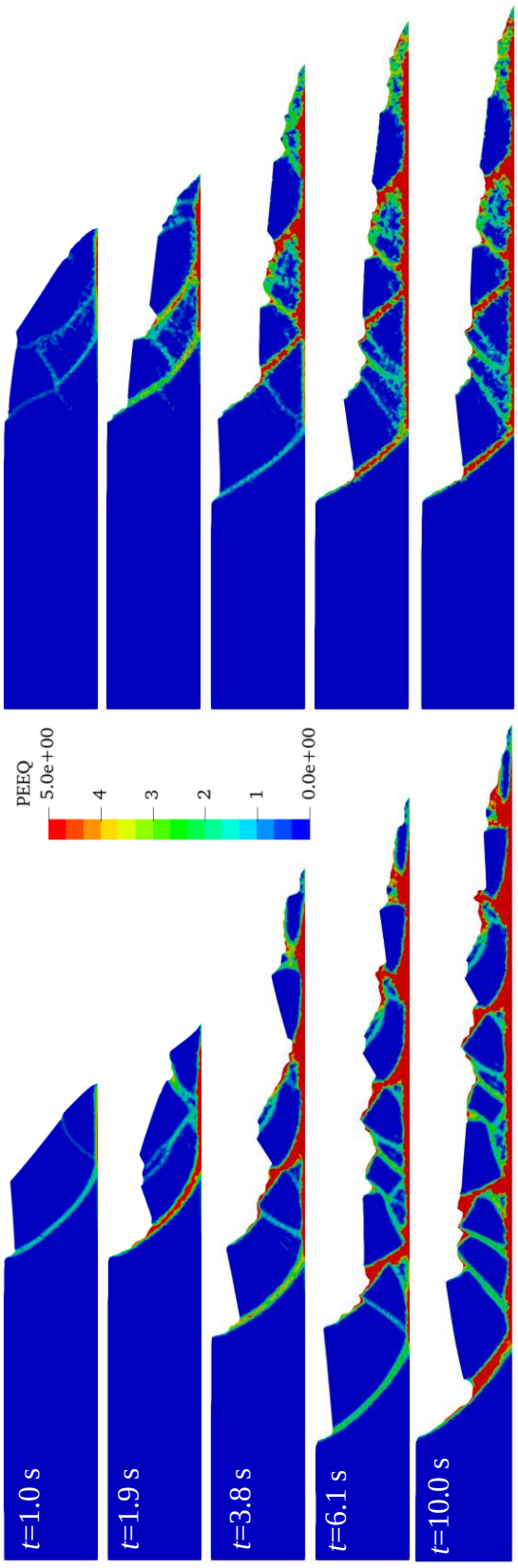

(a) SNS-PFEM

(b) NS-PFEM

Fig. 18 Retrogressive failure process of the slope at different calculation times

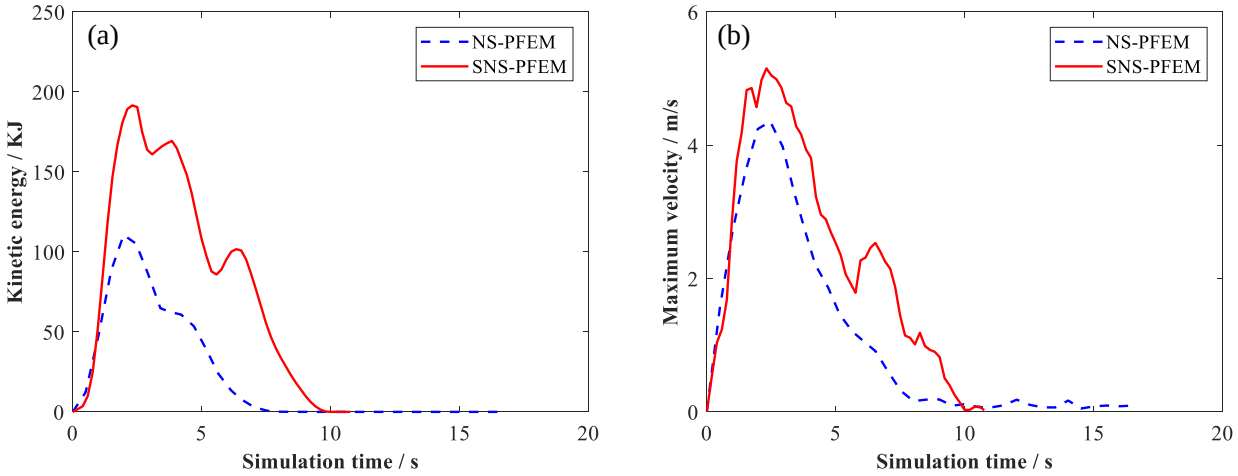

Fig. 19 Evolution of kinematic energy and maximum velocity of progressive slope failure

The collapse process and development of retrogressive failures within the slope is illustrated in Fig. 18, with the coloured contours representing the accumulated equivalent plastic strain. As illustrated, for both simulations, when the first retrogressive collapse moves far from the new slip surface, the second retrogressive collapse occurs, after which a third retrogressive collapse follows. The difference is that the block is complete, and its edges clear, for the SNS-PFEM simulation. Conversely, the temporal instability of the NS-PFEM leads to a fragmented soil block with noise and burrs in contours. Similar findings have been made by various other researchers [25, 28].

Another interesting phenomenon is that both run-out and retrogression distances for the SNS-PFEM simulation exceed those for the NS-PFEM simulation. It can be clearly found in Fig. 19 that the values of kinetic energy and maximum velocity for the SNS-PFEM simulation exceed those for the NS-PFEM simulation. Based on results of previous cases, the NS-PFEM solution is ‘‘overly soft’’ while the SNS-PFEM can give a close-to-exact solution. Under the same external work (i.e., gravitational loading for this case), the strain energy generated by NS-PFEM is larger than that of SNS-PFEM. As a result, the kinetic energy of NS-PFEM is smaller than that of SNS-PFEM, which reveals the result in Fig. 19. Note that the run-out and retrogression distances are affected by the model parameters, the interface friction coefficient, and even the adopted constitutive model.

For the same case with same mesh, the CPU time for the SNS-PFEM simulation was 115 min and for the NS-PFEM simulation was 62 min. Although CPU time for the NS-PFEM simulation was twice that for the SNS-PFEM simulation, neither time was unacceptably long.

The presented results indicate that the proposed SNS-PFEM with a strain-softening material model can well simulate retrogressive failure. The added stabilisation term can cure the temporal instability of the NS-PFEM, giving the SNS-PFEM remarkable and indeed superior convergence properties, without volumetric locking, with high levels of computational accuracy and efficiency, and with spatial and temporal stability.

~~4. Extension of the SNS-PFEM for hydromechanical analysis~~

~~This part presents the development……~~

4 Conclusions

A stable node-based smoothed particle finite element method (SNS-PFEM) for solving geotechnical large deformation problems has been developed. Compared with the original NS-PFEM, the strain in the smooth domain is linear when considering the strain gradient by integrating the first derivatives of the shape function on the boundary of the smooth domain. An additional stabilisation term was added to the internal force by adding four temporary integration points to capture uneven distribution of stress in the smooth domain. The performance of the proposed SNS-PFEM was ~~first~~ validated ~~using two benchmark tests on elastic material and three cases on elastoplastic material~~ based on two kinds of tests: (a) using two benchmark tests (i.e. cantilever beam and infinite plate with a circular hole) on elastic material to examine the convergence and accuracy of SNS-PFEM; (b) using three representative elastoplastic tests (i.e. cavity expansion, penetration of a rigid footing and progressive landslide) to examine the performance of SNS-PFEM on solving large deformation in terms of accuracy and temporal instability. All results demonstrated that the proposed SNS-PFEM can solve the 'overly soft' problem associated with the NS-PFEM and the SNS-PFEM had a 'close to exact' stiffness, thereby curing the temporal instability of the NS-PFEM. Accordingly, the

SNS-PFEM can be a powerful numerical method for use in solving large deformation problems of geotechnics.

~~To extend the application of the SNS-PFEM, a coupled hydromechanical SNS-PFEM with *v*–*w* formulation was then developed. A simple water pore pressure stabilisation scheme based on IDA interpolation was proposed and integrated. The proposed coupled SNS-PFEM was validated by three cases with good performance: (1) a 1D consolidation test, (2) a 1D dynamic consolidation test and (3) 2D wave propagation. Finally, the proposed coupled SNS-PFEM was applied to simulate the Selborne cutting slope experiment, demonstrating its outstanding performance. Accordingly, the SNS-PFEM can be a powerful numerical method for use in solving large deformation problems of geotechnics.~~

Further work will focus on the 3D extension of the method and the implementation of advanced constitutive models for analysing complex geotechnical structures.

Acknowledgements

This research was financially supported by the Research Grants Council (RGC) of Hong Kong Special Administrative Region Government (HKSARG) of China (Grant No.: R5037-18F), the Natural Science Foundation of Guangdong Province of China (Grant No.: 2018A030313897), Research Institute for Sustainable Urban Development of The Hong Kong Polytechnic University (Grant No: 1-BBWE), and the Postdoc Matching Fund Scheme of the Hong Kong Polytechnic University (Grant No: W14H).

Reference

[1] E. Onate, S.R. Idelsohn, M.A. Celigueta, R. Rossi, Advances in the particle finite element method for the analysis of fluid–multibody interaction and bed erosion in free surface flows, Comput Methods Appl Mech Eng, 197 (2008) 1777-1800.

[2] E. Oñate, S.R. Idelsohn, F. Del Pin, R. Aubry, The particle finite element method—an overview, Int. J. Comput. Methods 1(2004) 267-307.

[3] X. Zhang, K. Krabbenhoft, D. Sheng, Particle finite element analysis of the granular column collapse problem, Granular Matter 16 (2014) 609-619.

[4] X. Zhang, K. Krabbenhoft, D. Sheng, W. Li, Numerical simulation of a flow-like landslide using the particle finite element method, Comput. Mech. , 55 (2015) 167-177.

[5] X. Zhang, E. Oñate, S.A.G. Torres, J. Bleyer, K. Krabbenhoft, A unified Lagrangian formulation for solid and fluid dynamics and its possibility for modelling submarine landslides and their consequences, Computer Methods in Applied Mechanics and Engineering, (2018).

[6] L. Monforte, M. Arroyo, J.M. Carbonell, A. Gens, Numerical simulation of undrained insertion problems in geotechnical engineering with the particle finite element method (PFEM), Computers and Geotechnics, 82 (2017) 144-156.

[7] L. Monforte, M. Arroyo, J.M. Carbonell, A. Gens, Coupled effective stress analysis of insertion problems in geotechnics with the Particle Finite Element Method, Computers and Geotechnics, 101 (2018) 114-129.

[8] L. Monforte, J.M. Carbonell, M. Arroyo, A. Gens, Performance of mixed formulations for the particle finite element method in soil mechanics problems, Computational Particle Mechanics, 4 (2017) 269-284.

[9] L. Monforte, P. Navas, J.M. Carbonell, M. Arroyo, A. Gens, Low‐order stabilized finite element for the full Biot formulation in soil mechanics at finite strain, Int. J. Numer. Anal. Methods Geomech. , 43 (2019) 1488-1515.

[10] X. Zhang, D. Sheng, S.W. Sloan, J. Bleyer, Lagrangian modelling of large deformation induced by progressive failure of sensitive clays with elastoviscoplasticity, Int. J. Numer. Methods Eng. , 112 (2017) 963-989.

[11] X. Zhang, S.W. Sloan, E. Oñate, Dynamic modelling of retrogressive landslides with emphasis on the role of clay sensitivity, Int. J. Numer. Anal. Methods Geomech. , 42 (2018) 1806-1822.

[12] W.-H. Yuan, K. Liu, W. Zhang, B. Dai, Y. Wang, Dynamic modeling of large deformation slope failure using smoothed particle finite element method, Landslides, (2020) 1-13.

[13] W.-H. Yuan, B. Wang, W. Zhang, Q. Jiang, X.-T. Feng, Development of an explicit smoothed particle finite element method for geotechnical applications, Computers and Geotechnics, 106 (2019) 42-51.

[14] W. Zhang, W. Yuan, B. Dai, Smoothed Particle Finite-Element Method for Large-Deformation Problems in Geomechanics, Int. J. Geomech. , 18 (2018) 04018010.

[15] W. Zhang, Z.-h. Zhong, C. Peng, W.-h. Yuan, W. Wu, GPU-accelerated smoothed particle finite element method for large deformation analysis in geomechanics, Computers and Geotechnics, 129 (2021) 103856.

[16] N. Guo, Z. Yang, W. Yuan, J. Zhao, A coupled SPFEM/DEM approach for multiscale modeling of large‐deformation geomechanical problems, Int. J. Numer. Anal. Methods Geomech. , (2020).

[17] Y.-F. Jin, Z.-Y. Yin, W.-H. Yuan, Simulating retrogressive slope failure using two different smoothed particle finite element methods: A comparative study, Eng. Geol. , 279 (2020) 105870.

[18] Y.-F. Jin, W.-H. Yuan, Z.-Y. Yin, Y.-M. Cheng, An edge-based strain smoothing particle finite element method for large deformation problems in geotechnical engineering, Int. J. Numer. Anal. Methods Geomech. , 44 (2020) 923-941.

[19] T. Vo-Minh, L. Nguyen-Son, A stable node-based smoothed finite element method for stability analysis of two circular tunnels at different depths in cohesive-frictional soils, Computers and Geotechnics, 129 (2021) 103865.

[20] S. Ren, G. Meng, J. Wang, L. Zhou, H. Zhao, A stabilized node-based smoothed radial point interpolation method for functionally graded magneto-electro-elastic structures in thermal environment, Compos. Struct. , 234 (2020) 111674.

[21] G. Liu, T. Nguyen-Thoi, K. Lam, A novel alpha finite element method (αFEM) for exact solution to mechanics problems using triangular and tetrahedral elements, Comput Methods Appl Mech Eng, 197 (2008) 3883-3897.

[22] Z.-Q. Zhang, G. Liu, Temporal stabilization of the node-based smoothed finite element method and solution bound of linear elastostatics and vibration problems, Comput. Mech. , 46 (2010) 229-246.

[23] C. Wu, Y. Wu, Z. Liu, D. Wang, A stable and convergent Lagrangian particle method with multiple nodal stress points for large strain and material failure analyses in manufacturing processes, Finite Elem. Anal. Des. , 146 (2018) 96-106.

[24] M. Puso, J. Chen, E. Zywicz, W. Elmer, Meshfree and finite element nodal integration methods, Int. J. Numer. Methods Eng. , 74 (2008) 416-446.

[25] H. Feng, X. Cui, G. Li, A stable nodal integration method with strain gradient for static and dynamic analysis of solid mechanics, Eng. Anal. Boundary Elem. , 62 (2016) 78-92.

[26] Y. Li, G.R. Liu, A novel node-based smoothed finite element method with linear strain fields for static, free and forced vibration analyses of solids, Applied Mathematics and Computation, 352 (2019) 30-58.

[27] Y. Li, G. Liu, Z. Feng, K. Ng, S. Li, A node-based smoothed radial point interpolation method with linear strain fields for vibration analysis of solids, Eng. Anal. Boundary Elem. , 114 (2020) 8-22.

[28] G. Chen, L. Qian, J. Ma, A gradient stable node-based smoothed finite element method for solid mechanics problems, Shock and Vibration, 2019 (2019).

[29] M. Nazem, D. Sheng, J.P. Carter, Stress integration and mesh refinement for large deformation in geomechanics, Int. J. Numer. Methods Eng. , 65 (2006) 1002-1027.

[30] Y.-F. Jin, Z.-Y. Yin, Z.-X. Wu, A. Daouadji, Numerical modeling of pile penetration in silica sands considering the effect of grain breakage, Finite Elem. Anal. Des. , 144 (2018) 15-29.

[31] J.S. Chen, C.T. Wu, T. Belytschko, Regularization of material instabilities by meshfree approximations with intrinsic length scales, Int. J. Numer. Methods Eng. , 47 (2000) 1303-1322.

[32] J.S. Chen, C.T. Wu, S. Yoon, Y. You, A stabilized conforming nodal integration for Galerkin mesh‐free methods, Int. J. Numer. Methods Eng. , 50 (2001) 435-466.

[33] G.-R. Liu, N.T. Trung, Smoothed finite element methods, CRC press, 2016.

[34] G. Liu, T. Nguyen-Thoi, H. Nguyen-Xuan, K.J.C. Lam, structures, A node-based smoothed finite element method (NS-FEM) for upper bound solutions to solid mechanics problems, 87 (2009) 14-26.

[35] W. Zeng, G. Liu, Smoothed finite element methods (S-FEM): an overview and recent developments, Archives of Computational Methods in Engineering, 25 (2018) 397-435.

[36] H. Yang, X. Cui, S. Li, Y. Bie, A stable node-based smoothed finite element method for metal forming analysis, Comput. Mech. , 63 (2019) 1147-1164.

[37] M. Hillman, J.S. Chen, An accelerated, convergent, and stable nodal integration in Galerkin meshfree methods for linear and nonlinear mechanics, Int. J. Numer. Methods Eng. , 107 (2016) 603-630.

[38] H. Feng, X. Cui, G. Li, A stable nodal integration method for static and quasi-static electromagnetic field computation, J. Comput. Phys. , 336 (2017) 580-594.

[39] Y. Li, G. Liu, J. Yue, A novel node-based smoothed radial point interpolation method for 2D and 3D solid mechanics problems, Computers & Structures, 196 (2018) 157-172.

[40] S. Ren, C. Na, G. Meng, B. Nie, L. Zhou, Stabilized node‐based smoothed radial point interpolation method for micromechanical analysis of the magneto‐electro‐elastic structures in thermal environment, Mathematical Methods in the Applied Sciences, (2020).

[41] H.-S. Yu, Cavity expansion methods in geomechanics, Springer Science & Business Media, 2000.

[42] L. Monforte, M. Arroyo, J.M. Carbonell, A. Gens, Numerical simulation of undrained insertion problems in geotechnical engineering with the Particle Finite Element Method (PFEM), Computers and Geotechnics, 82 (2017) 144-156.

[43] W.T. Sołowski, S.W. Sloan, Evaluation of material point method for use in geotechnics, International Journal for Numerical and Analytical Methods in Geomechanics, 39 (2015) 685-701.

[44] M. Kardani, M. Nazem, J.P. Carter, A.J. Abbo, Efficiency of high-order elements in large-deformation problems of geomechanics, International Journal of Geomechanics, 15 (2015) 04014101.

[45] W. Sołowski, S. Sloan, Evaluation of material point method for use in geotechnics, Int. J. Numer. Anal. Methods Geomech. , 39 (2015) 685-701.

[46] M. Kardani, M. Nazem, J. Carter, A. Abbo, Efficiency of high-order elements in large-deformation problems of geomechanics, Int. J. Geomech. , 15 (2014) 04014101.

[47] L. Prandtl, Hauptaufsätze: Über die Eindringungsfestigkeit (Härte) plastischer Baustoffe und die Festigkeit von Schneiden, ZAMM - Journal of Applied Mathematics and Mechanics / Zeitschrift für Angewandte Mathematik und Mechanik, 1 (1921) 15-20.

[48] G.G. Meyerhof, The Ultimate Bearing Capacity of Foudations, Geotechnique, 4 (1951) 301-332.

[49] A. Locat, S. Leroueil, S. Bernander, D. Demers, H.P. Jostad, L. Ouehb, Progressive failures in eastern Canadian and Scandinavian sensitive clays, Can. Geotech. J., 48 (2011) 1696-1712.

[50] A. Yerro, MPM modelling of landslides in brittle and unsaturated soils. Ph. D. thesis, Universitat Politècnica de Catalunya, 2015.

[51] Z.Y. Yin, J.H. Yin, H.W. Huang, Rate-Dependent and Long-Term Yield Stress and Strength of Soft Wenzhou Marine Clay: Experiments and Modeling, Marine Georesources & Geotechnology, 33 (2015) 79-91.

[52] Z.Y. Yin, M. Karstunen, C.S. Chang, M. Koskinen, M. Lojander, Modeling Time-Dependent Behavior of Soft Sensitive Clay, J. Geotech. Geoenviron. Eng., 137 (2011) 1103-1113.

[53] S. Bernander, A. Kullingsjö, A.S. Gylland, P.-E. Bengtsson, S. Knutsson, R. Pusch, J. Olofsson, L. Elfgren, Downhill progressive landslides in long natural slopes: triggering agents and landslide phases modeled with a finite difference method, Can. Geotech. J., 53 (2016) 1565-1582.

[54] A. Locat, S. Leroueil, A. Fortin, D. Demers, H.P. Jostad, The 1994 landslide at Sainte-Monique, Quebec: geotechnical investigation and application of progressive failure analysis, Can. Geotech. J., 52 (2015) 490-504.